CrossMark

Influence of Initial Microstructure on the Strengthening Effect of Extruded Mg–8Sn–4Zn–2Al Alloys

Yang Bai[1] · Wei-Li Cheng[1,2,3] · Shi-Chao Ma[1] · Jun Zhang[1] · Chen Guo[1] · Yao Zhang[1]

Abstract The Mg–8Sn–4Zn–2Al (TZA842, in wt%) alloys with different initial microstructure (as-cast-AC and homogenization treatment-HT) subjected to hot extrusion. Also, the strengthening responses to AC and HT for the extruded TZA842 alloys were reported. The results revealed that the alloy subjected to HT shows finer grain size, more homogenous microstructure and weaker basal texture than those of counterpart subjected to AC. In addition, compared with TZA842-AC alloy, precipitates were finer and uniformly dispersed in TZA842-HT owing to the utilization of HT. Moreover, the TZA842-HT alloy showed higher yield strength of 200 MPa, ultimate tensile strength of 290 MPa and elongation (EL) of 17.9% than those of TZA842-AC, which was mainly attributed to the combined effects of grain boundary strengthening, precipitation strengthening, solid solution strengthening and weak texture. Strengthening mechanism for both alloys was discussed in detail.

KEY WORDS: Mg–Sn alloy; Extrusion; Microstructure; Tensile property; Strengthening mechanism

1 Introduction

Nowadays, Mg–Sn-based alloys with a high Sn content have received considerable attention owing to their excellent potential for developing extrusion alloy products with good creep resistance [1]. This is mainly attributed to the

✉ Wei-Li Cheng
  chengweili7@126.com

1 School of Materials Science and Engineering, Taiyuan University of Technology, Taiyuan 030024, China

2 Shanxi Key Laboratory of Advanced Magnesium-Based Materials, Taiyuan University of Technology, Taiyuan 030024, China

3 Key Laboratory of Interface Science and Engineering in Advanced Materials, Ministry of Education, Taiyuan University of Technology, Taiyuan 030024, China

formation of high melting point (770 °C) Mg_2Sn phase, which could prevent the occurrence of hot shortness during hot working. However, the tensile properties of the binary Mg–Sn alloy are still poor due to the coexistence of coarse and fine Mg_2Sn particles within the α-Mg matrix [2]. Thus, several microalloying elements, such as Zn [3], Na and Li, Cu and Hf [4], are added into Mg–Sn-based alloys in order to refine the Mg_2Sn precipitates. Among all above-mentioned elements, Zn has been found not only to promote the formation of Mg_2Sn precipitates on the non-basal planes of Mg matrix but also to segregate at the Mg_2Sn/Mg interface [5]. Furthermore, many studies have been reported that extruded Mg–Sn–Zn–Al (TZA) series alloys exhibit an enhanced tensile yield strength compared to that of commercial Mg–Al and Mg–Zn-based alloys [1, 6].

As well known, grain refinement is an effective way to improve the strength and ductility simultaneously. It has been reported that ultrafine-grained materials could be prepared by extrusion and ECAP, which can effectively

Springer

improve the tensile properties of Mg alloys [7, 8]. Generally, Mg extrusion products are generally fabricated by the following processes: casting, HT and hot extrusion. Controlling initial microstructure via different pretreatments prior to extrusion processing is just as important as extrusion parameters in determining dynamic precipitation and recrystallization behavior during the extrusion process. To date, the initial microstructures with undissolved particles have caused considerable controversy. For example, Kim et al. [9] reported that the presence of undissolved particles in a billet can prevent the formation of precipitates during extrusion, which, in turn, decreases the strength of the extruded Mg alloys. However, Park et al. [10] indicated that the remaining particles in a homogenized billet can increase the fraction of DRXed grains, resulting in a weak texture. Thus far, there has been no in-depth study on microstructural characteristics and tensile properties of extruded Mg–Sn based alloys. Therefore, the aim of present investigation is to reveal the effects of initial microstructure on the tensile properties of the extruded TZA842 alloys. Moreover, the strengthening mechanisms of the extruded alloy subjected to HT were calculated quantitatively using the alloy subjected to AC as benchmark.

2 Experimental

The ingots with nominal composition Mg–8Sn–4Zn–2Al (wt%) (TZA842) were prepared by melting commercially pure Mg (99.9 wt%), Sn (99.93 wt%), Zn (99.99 wt%) and Al (99.99 wt%) in an electrical resistance furnace with the protection of a mixture of gaseous CO_2 and SF_6. The melt was poured into a preheated steel mold (200 °C). The chemical composition of the billets was subsequently measured by inductively coupled plasma spectrometry (ICP: Thermo Xseries II) as being Mg–7.95Sn–4.02Zn–1.98Al (wt%). HT was conducted at 320 °C for 3 h and then at 450 °C for 24 h, followed by water quenching. The samples (40 mm in diameter and 50 mm in length) were machined and directly extruded at an initial billet temperature of 300 °C, a ram speed of 0.1 mm s^{-1} and an extrusion ratio of 16. The extruded TZA842 alloys subjected to AC and HT prior to extrusion were marked as TZA842-AC and TZA842-HT alloys, respectively.

Phase identification and macro-textures of the extruded samples were performed with a Rigaku D/MAX-2500PC X-ray diffractometer (XRD). The microstructure of the specimens was examined by a Leica 2700 M optical microscope (OM) and a Mira 3XMU scanning electron microscope (SEM) equipped with an energy-dispersive spectrometer (EDS). The average sizes and the amounts of both DRXed grains and precipitates were calculated from the number and/or area fraction using three micrographs by the Image-Pro plus 6.0 software. Tensile specimens (18 mm gauge length × 4 mm gauge width × 2 mm gauge thickness) were cut from the extruded rods along the extrusion direction (ED). Tensile tests were then carried out at room temperature using a DNS100 electric testing machine with an initial strain rate of 1×10^{-3} s^{-1}. Tensile tests of each specimen were repeated three times, and the average values of these measurements were used in this study.

3 Results and Discussion

3.1 Phase Analysis by XRD

Figure 1 shows the XRD patterns of the TZA842 alloys under various conditions. It was apparent that the TZA842 alloys mainly consisted of α-Mg, Mg_2Sn and $Mg_{32}(AlZn)_{49}$ phases, and no other phase was detected. After HT, the intensities of the Mg_2Sn and $Mg_{32}(AlZn)_{49}$ peaks decreased, implying that most of the second phases have dissolved into the α-Mg matrix. In addition, the peak intensities of the second phases were enhanced after extrusion obviously, indicating the occurrence of dynamic precipitation during extrusion, which usually observed in Mg–Sn-based extrudes [11, 12]. Furthermore, the peaks corresponding to Mg_2Sn in the TZA842-HT alloy were relatively high compared to that in the TZA842-AC. It is well known that during HT prior to extrusion, most of the insoluble coarse Mg_2Sn particles in the casting process were dissolved into the matrix; in other words, most of the Sn elements were present in the solid solution states in the matrix. This means that the dynamic precipitation rate of
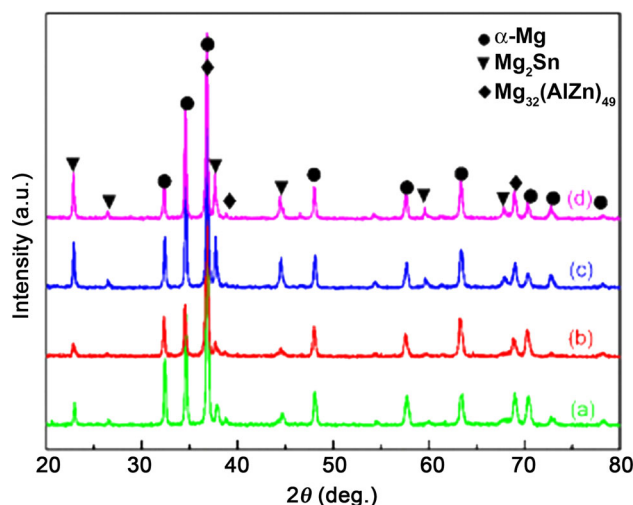

Fig. 1 XRD patterns of the TZA842 alloys: **a** as-cast, **b** as-homogenized, **c** TZA842-AC, **d** TZA842-HT

Mg_2Sn particles was stronger in the TZA842-HT alloy than in the TZA842-AC [6].

3.2 As-Cast and As-Homogenized Microstructures

Figure 2 shows the microstructures of both as-cast and as-homogenized TZA842 alloys. The as-cast alloy (Fig. 2a) exhibited a typical dendritic microstructure, and the average secondary dendrite arm spacing was $\sim$ 22.4 μm. After homogenization as shown in Fig. 2b, the equiaxial grains with an average grain size of $\sim$ 88.2 μm and a few undissolved particles distributed at the grain boundaries and grain interiors could be observed. According to the SEM (Fig. 2c, d) and EDS results in Table 1, these second phase particles in the AC condition were identified as Mg_2Sn and $Mg_{32}(AlZn)_{49}$ phases with volume fraction of $\sim$ 10.2%. It should be note that $Mg_{32}(AlZn)_{49}$ phase was located between α-Mg + Mg_2Sn eutectic and dissociative Mg_2Sn phases, indicating that the formation of Mg_{32} $(AlZn)_{49}$ phase lags behind the eutectic phases during

Table 1 EDS results of TZA842 alloys

Position	Element				Possible compound
	Mg	Sn	Zn	Al	
A	72.8	27.2	–	–	α-Mg + Mg_2Sn
B	60.1	39.9	–	–	Mg_2Sn
C	39.7	–	44.5	15.8	$Mg_{32}(AlZn)_{49}$
D	51.1	48.9	–	–	Mg_2Sn
E	54.1	45.9	–	–	Mg_2Sn
F	40.9	–	43.1	16.0	$Mg_{32}(AlZn)_{49}$
G	59.0	41.0	–	–	Mg_2Sn
H	41.3	–	42.5	16.2	$Mg_{32}(AlZn)_{49}$

solidification [3]. Similarly, the formation of Mg_x $(AlZn)_{1-x}$ phase in Mg–8Sn–xAl(2,3)–1Zn and Mg–7Sn–5Zn–2Al alloys has been reported, indicating that the formation of Mg–Al–Zn phase is possible in Mg–Sn–Zn–Al alloy system with relatively low Zn and Al contents. While
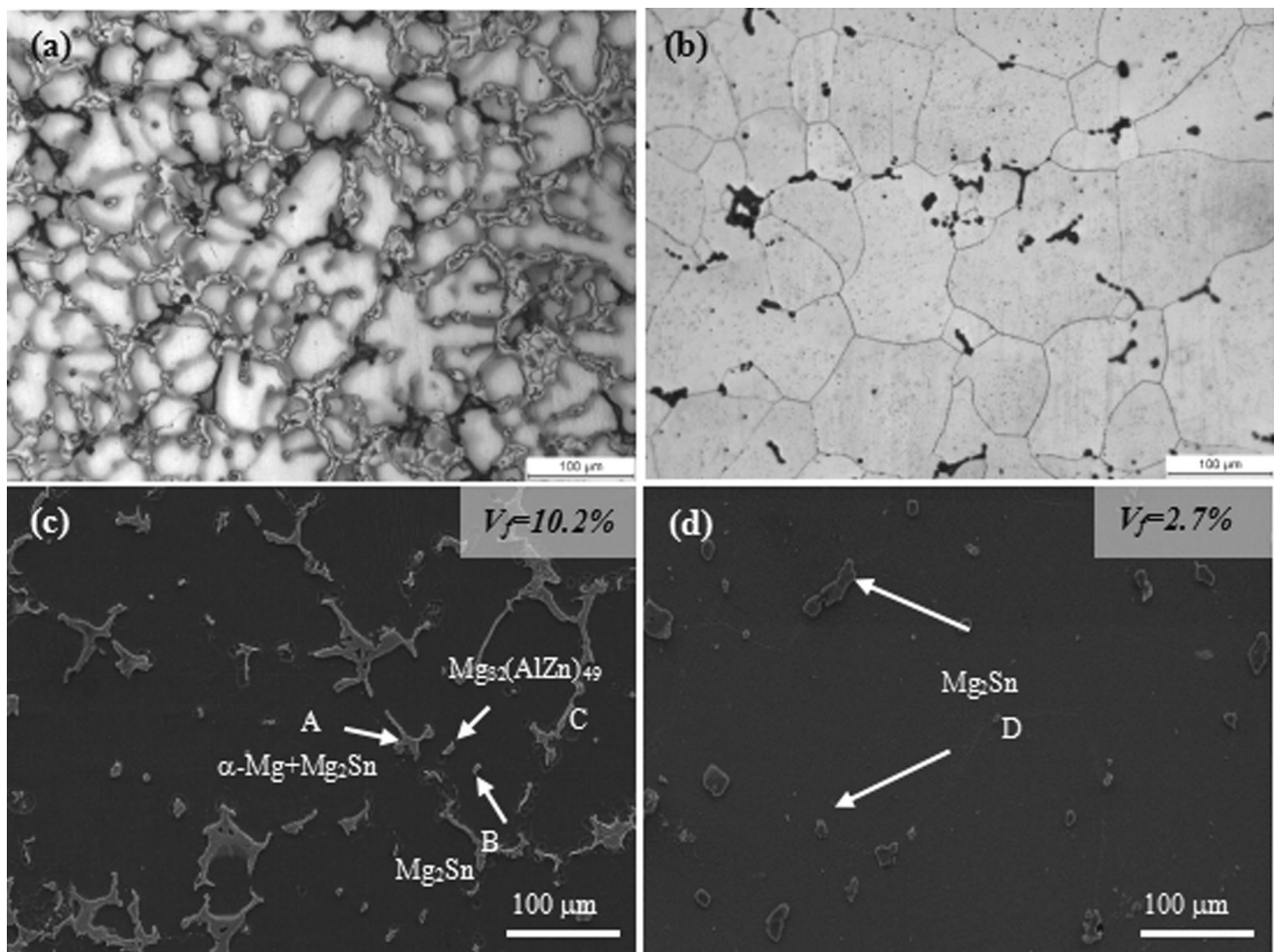

Fig. 2 OM and SEM images of TZA842 alloys prior to extrusion in different states: **a**, **c** as-cast **b**, **d** as-homogenized

in HT condition, the remained particles were mainly composed of Mg$_2$Sn owing to its high melting point than that of Mg$_{32}$(AlZn)$_{49}$, and the totally volume fraction of remain particles was ~ 2.7%. These differences in the initial microstructure will result in various extrusion morphology as well as related tensile properties, which will be discussed in the following sections.

3.3 Microstructures of the Extruded Alloys

Figure 3 shows the optical micrographs of the extruded TZA842 alloys taken from the planes parallel to the ED. The extruded alloys exhibited a typical bimodal grain structure consisting of fine DRXed grains and coarse unDRXed regions elongated along the ED, while the volume fraction of DRXed grains (f_{DRX}) in the TZA842-HT alloy (98.2%) was higher compared to that of the TZA842-AC one (93.3%) (Fig. 3a, b). In addition, the recrystallized grains in the former alloy had the average DRXed grain size of ~ 1.73 µm, which was finer than that of the latter

one (~ 3.71 µm) (Fig. 3c, d). The detailed microstructural characteristics are also provided in Table 2. Thus, more homogenous microstructure could be obtained in TZA842-HT alloy compared with TZA842-AC, indicating that the initial microstructure plays an important role in DRX processing.

The SEM images and particles size distribution of extruded TZA842 alloys are shown in Fig. 4. It was obvious that undissolved particles in AC and HT conditions were broken into fragments and aligned along the ED during extrusion process (Fig. 4a, b). EDS analysis (Table 1) indicated these undissolved secondary phases were Mg$_2$Sn and Mg$_{32}$(AlZn)$_{49}$, respectively. Furthermore, it is well known that the particles having 1–10 µm diameter can act as nucleation sites for DRX by producing local inhomogeneity in strain energy during extrusion process, which is defined as particle-stimulated nucleation (PSN) [11, 13]. For a quantitative analysis of PSN effect, the size distribution and number of the particles large than 1 µm in size were measured for both alloys (Fig. 4c). It could be
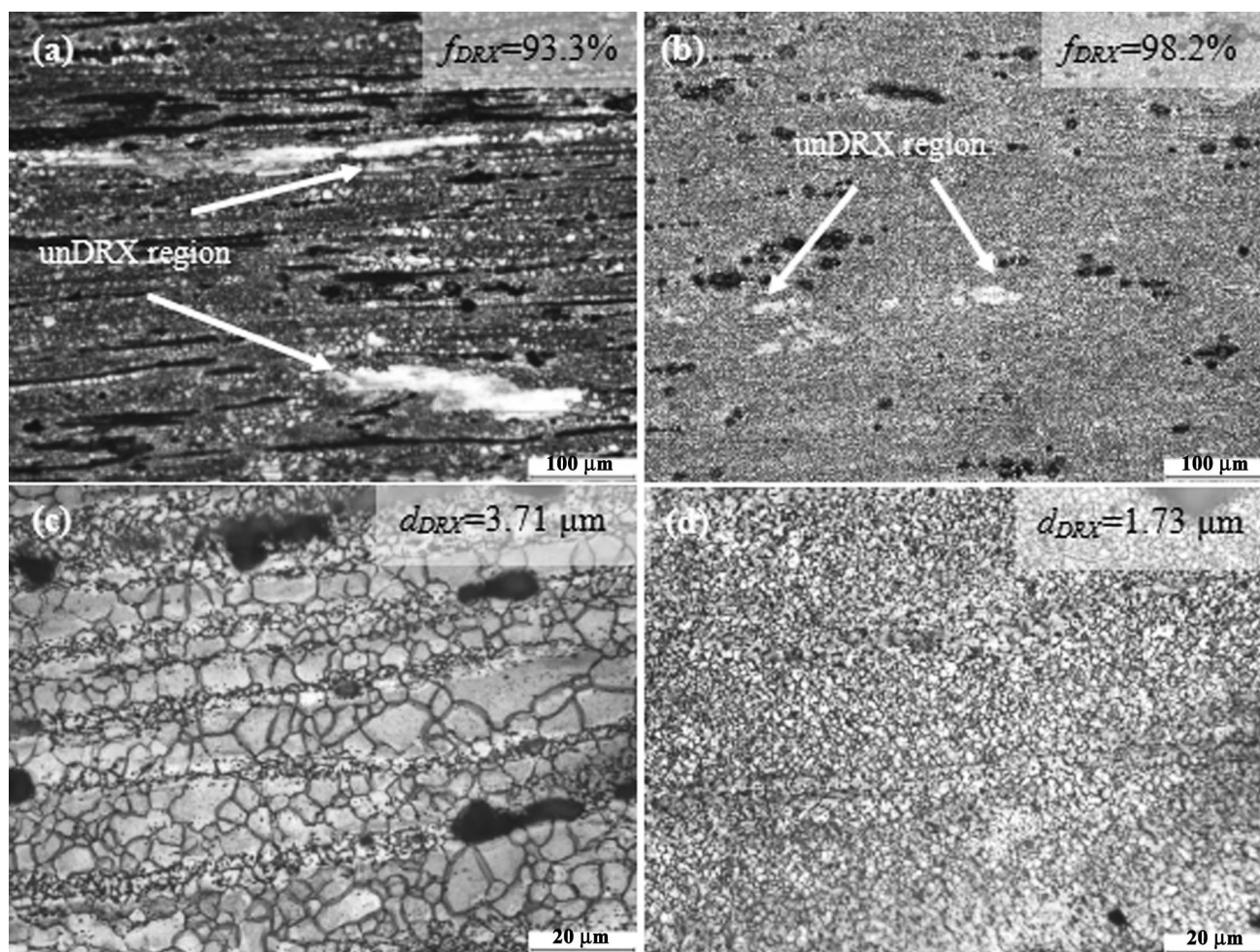

Fig. 3 OM images of extruded TZA842 alloys in different states: **a, c** TZA842-AC **b, d** TZA842-HT

Y. Bai *et al.*: Acta Metall. Sin. (Engl. Lett.), 2018, **31**, 487–495

491

Table 2 Microstructural characteristics and tensile properties of extruded TZA842 alloys

State	Microstructure				Tensile properties			
	f_{DRX} (%)	d_{DRX} (µm)	f_P (%)	d_P (µm)	YS (MPa)	UTS (MPa)	EL (%)	n
TZA842-AC	93.3	3.71	2.3	0.33	145 ± 3	216 ± 4	15.2 ± 0.3	0.19
TZA842-HT	98.2	1.78	10.7	0.23	200 ± 2	290 ± 2	17.9 ± 0.2	0.24

f_{DRX} and d_{DRX} represent the volume fraction and average grain size of DRX grains, respectively. f_P and d_P represent the volume fraction and average grain size of precipitates, respectively

YS, UTS and EL represent tensile yield strength, ultimate tensile strength, and elongation. n represents work-hardening exponents

found that the number of particles in the 1–10 µm in the TZA842-HT alloy were larger than that of TZA842-AC one, and thus led to an increase in the DRX volume fraction of the extruded alloy by an enhanced PSN effect.

In addition, it could be seen that nano-size precipitates were uniformly distributed along DRXed grain boundaries and within the grains interiors in the TZA842-HT alloy as compared with the TZA842-AC alloy (Fig. 4d, e). Measurements indicated that the average size (d_P) and volume fractions (f_P) of the precipitates are 330 nm, 2.3% and 230 nm and 10.7% for both alloys, respectively. This suggested that the dynamic precipitation rate of the TZA842 alloy could be enhanced by HT before extrusion. It is well known that during homogenization treatment prior to extrusion, most of the insoluble coarse particles in the casting process are dissolved into the matrix, and in other words, most of Sn, Zn and Al elements are presented in the solid solution states in the matrix. In the following extrusion process, this will cause more fine Mg_2Sn and $Mg_{32}(Al, Zn)_{49}$ precipitates. Furthermore, according to previous reports, fine Mg_2Sn phases belong to non-basal plane precipitates in extruded Mg–8Sn-based alloys, which can effectively hinder basal dislocation slip [6]. In addition, the interface between the $Mg_x(AlZn)_{1-x}$ phase and the matrix is a semi-coherent interface in extruded Mg–Sn–Zn–Al alloys [11]. Therefore, the above-mentioned fine precipitates play an important role in restricting grain growth by grain boundary pinning effect [6, 14], resulting in the average size of DRXed grains decreased from ∼ 3.71 µm (TZA842-AC) to ∼ 1.78 µm (TZA842-HT) as the fraction of fine precipitates increased.

The (0002) pole figures of the extruded TZA842 alloys are presented in Fig. 5. The TZA842-AC alloys exhibited a basal texture in which (0002) basal planes are parallel to the ED, while the basal plane of the TZA842-HT alloy interval to the ED around ∼ 12°. Note that the texture intensity of TZA842-HT alloy was relatively low compared to that of TZA842-AC. Such textural weakening could be understood by considering the aforementioned difference in DRX fraction and dynamic precipitates. It has been reported that DRX grains have different textures from

unDRXed grains in Mg alloys, demonstrating that the texture of the DRXed grains is much more randomized than that of the unDRXed grains [15]. Thus, the textural weakening of TZA842-HT alloy could be attributed to increasing volume fraction of DRXed grains.

Furthermore, dynamic precipitates can provide more randomly oriented nuclei and thus significantly weaken the basal plane texture in Mg alloys [16]. Namely, the larger amount of dynamic precipitates led to the weaker basal plane texture. As exhibited in Fig. 4d, e, the TZA842-HT alloy exhibited abundant of dynamic precipitates, resulting in a weaker basal plane texture, which is foreseeable.

3.4 Tensile Properties of the Extruded Alloys

Tensile engineering stress–strain curves of the extruded TZA842 alloys are shown in Fig. 6a, and the corresponding values are summarized in Table 2. The TZA842-HT alloy exhibited tensile properties superior to those of the TZA842-AC. The yield strength (YS), ultimate tensile strength (UTS) and elongation (EL) for the TZA842-HT alloy were 200, 290 MPa and 17.9%, respectively, whereas they were 145, 216 MPa and 15.2% for the TZA842-AC.

Figure 6b gives the related work-hardening rate ($\theta = \frac{d\sigma}{d\varepsilon}$, where σ is true stress) versus the net flow stress ($\sigma - \sigma_{0.2}$) curves for the extruded TZA842 alloys according to converting of engineering stress–strain to true stress–strain curves. Firstly, θ decreased sharply after yielding, exhibiting stage III hardening behavior (dynamic recovery stage); then θ became small, indicating that the hardening stage IV (large-strain work-hardening stage) occurred. These similar stages could be observed in both alloys. However, the TZA842-HT alloy exhibited a higher work-hardening rate in comparison with the TZA842-AC, which was related to the fraction of dispersed precipitates (10.7 and 2.3% for both alloys). Normally, based on interacting effect between dislocations and precipitates, nano-size precipitates lead to the increment of the required stress to move dislocations, and therefore resulted in a higher work-hardening rate [17]. Furthermore, the work-hardening
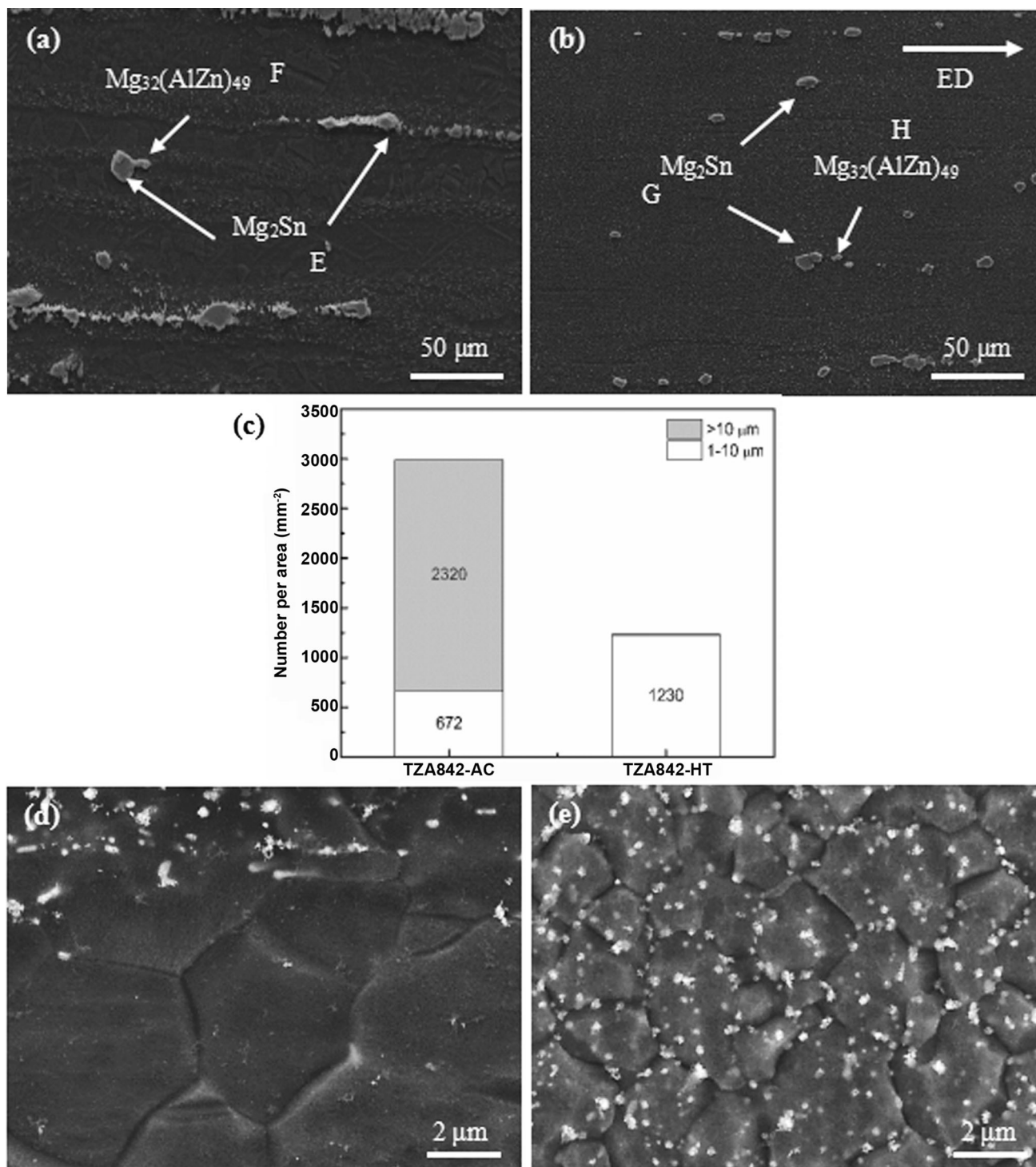
Fig. 4 SEM images of extruded TZA842 alloys: **a**, **d** TZA842-AC, **b**, **e** TZA842-HT, **c** particle size distribution in both alloys

exponents (n) acquired from the Hollomon equation, $\sigma = K\varepsilon^n$, are 0.19 and 0.24 for the TZA842-AC and TZA842-HT alloys, respectively. Generally, higher n value led to a lower sensitivity to strain localization and hence a greater EL [18].

It is generally believed that the yield strength of wrought magnesium alloys is associated with grain size, texture intensity, dynamic precipitate particles and solute atoms.

Firstly, the influence of the grain size on the YS, defined as σ_g, could be calculated by the Hall–Petch relation [11]:

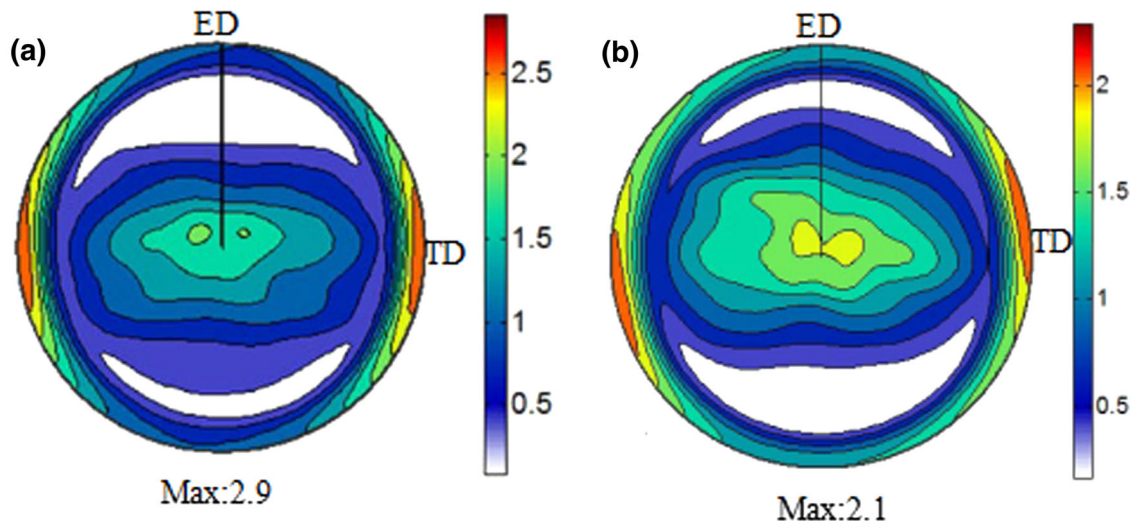Y. Bai *et al.*: Acta Metall. Sin. (Engl. Lett.), 2018, **31**, 487–495

493

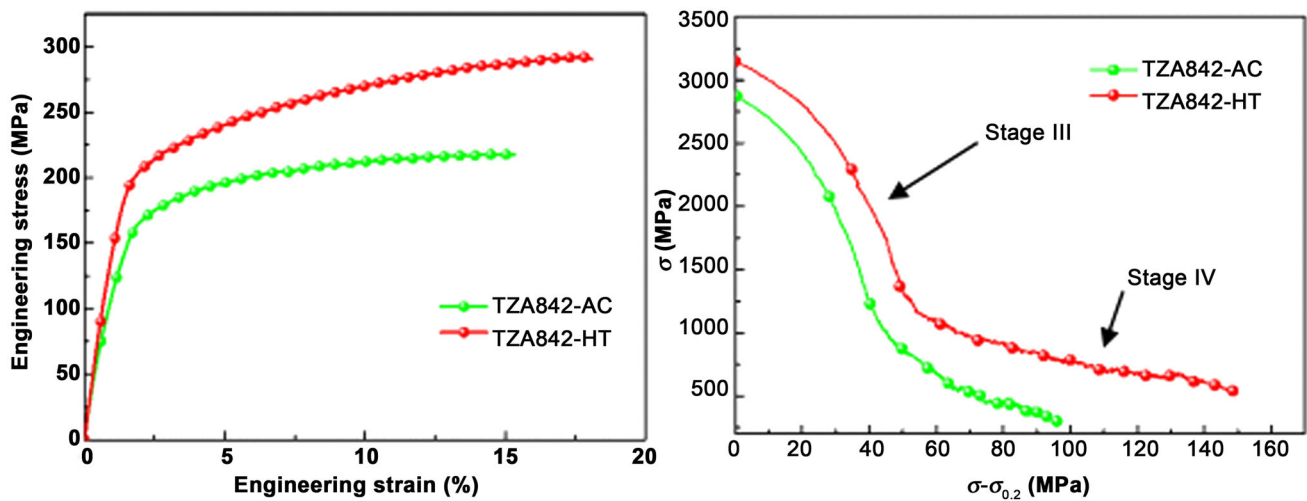**Fig. 5** The (0002) pole figures of the extruded alloys: **a** TZA842-AC and **b** TZA842-HT

Fig. 6 a Tensile engineering stress–strain curves and **b** work-hardening rate (θ) as function of net flow stress ($\sigma - \sigma_{0.2}$) of extruded TZA842 alloys

$$\sigma_g = \sigma_0 + kd^{-1/2}. \tag{1}$$

where σ_g is the YS, k is an experimental constant and d is the average grain size. Previous studies indicated that k value of 280 MPa$\sqrt{\mu m}$ is suitable for Mg–Sn-based alloys [19]. Therefore, the difference in YS between TZA842-HT and TZA842-AC alloys could be calculated by Eq. (2) as follows:

$$\Delta\sigma_g = k\left(d_{TZA842-HT}^{-1/2} - d_{TZA842-AC}^{-1/2}\right). \tag{2}$$

The calculated $\Delta\sigma_g$ was approximately 64.5 MPa due to grain refinement from $d = 3.71$–1.78 μm.

Secondly, the strong basal plane texture developed in the extruded alloys, which was thought to be beneficial to the improvement of the strength [20]. The contribution of texture to YS (σ_t) could be expressed as Eq. (3):

$$\sigma_t = M\tau_0. \tag{3}$$

where M is an orientation factor related to the basal texture in the material, and τ_0 is the critical resolved shear stress (CRSS) for the operative slip system. Previous study suggested that, for Mg–Sn-based alloys, the value of M could be calculated by taking 6.5 times the maximum texture intensity of (0002) pole figure [19]. Therefore, M was ~ 13.7 and ~ 18.9 (for maximum pole figure intensities ~ 2.1 and 2.9) for the TZA842-HT and TZA842-AC alloys, respectively. The increase in strength between TZA842-HT and TZA842-AC alloys could be described by following Eq. (4):

$$\Delta\sigma_t = (M_{TZA842-HT} - M_{TZA842-AC})\tau_0. \tag{4}$$

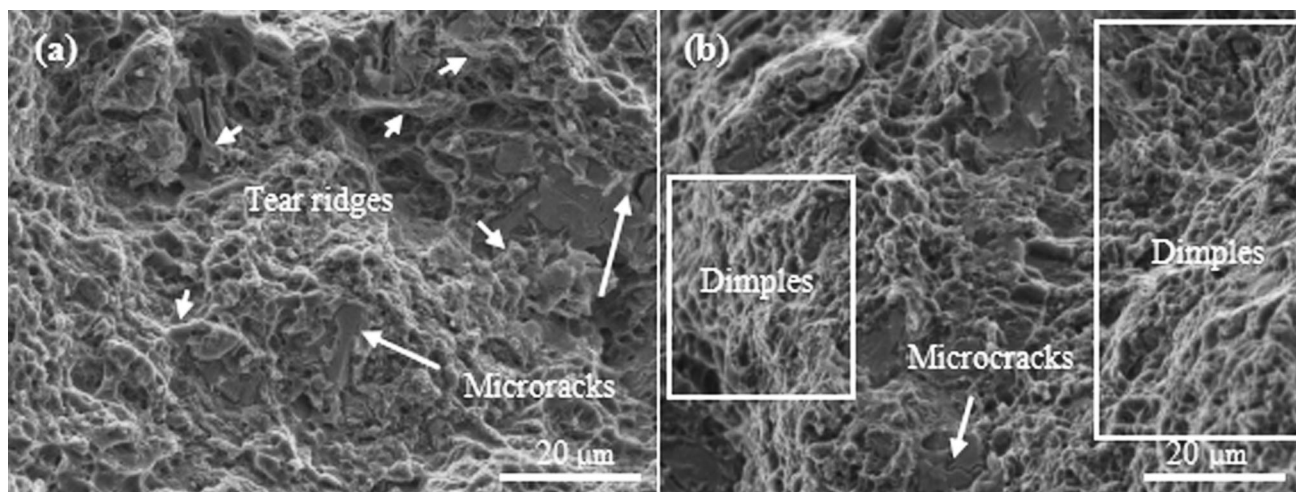It also had been reported that τ_0 values for basal slip, prismatic slip, pyramidal slip and tension twinning of Mg

Fig. 7 SEM images of the extruded alloys: **a** TZA842-AC and **b** TZA842-HT

at elevated temperatures range from 0.6 to 4 MPa [21]. Basal < a > slip could be easily activated at relatively low temperature due to its low CRSS. Previous report indicated that the CRSS for basal slip in pure Mg was 0.5 MPa [21]. In addition, the effects of solutes on CRSS for basal slip were 3.2 MPa [22]. In this work, the value of τ_0 was supposed to be 3.7 due to the lack of information on Mg–Sn-based alloys at room temperature. Therefore, the calculated $\Delta\sigma_t$ was ~ -19 MPa.

Thirdly, fine particles dynamically precipitated during extrusion can enhance the YS (σ_P) by the Orowan mechanism [23, 24], meaning that the particles can serve as obstacles to dislocation movement. Thus, the increase in YS could be calculated by Eq. (5):

$$\sigma_P = M \frac{0.4\,Gb}{\pi\sqrt{1-\upsilon}} \frac{\ln(2\bar{r}/b)}{\lambda}. \tag{5}$$

where $M = 1.25$ is the Taylor factor, $G = 16.6$ GPa is the Shear modulus, $b = 0.32$ nm is Burgers vector, $\upsilon = 0.267$ is the Poisson ratio, $\bar{r} = \sqrt{\frac{2}{3}}r$, where r is the radius of the precipitate, and $\lambda = 2\bar{r}\left(\sqrt{\pi/4f} - 1\right)$, where f is the volume fraction of precipitates. According to above result, the average sizes and fraction of fine particles in TZA842-AC and TZA842-HT alloys were determined to be 330 nm, 2.3% and 230 nm, 10.7%, respectively. Therefore, the σ_P can be calculated as ~ 2.8 and ~ 9.2 MPa, respectively, and the distinction in σ_P could be determined as follows:

$$\Delta\sigma_p = \sigma_{p-HT} - \sigma_{p-AC}. \tag{6}$$

Thus, $\Delta\sigma_p$ is ~ 6.4 MPa in this case.

Finally, solute atoms such as Sn, Zn and Al also have a prominent effect on the YS (σ_S). As the main elements in TZA842 alloys, the weight percent of Sn, Zn and Al was 7.95, 4.02 and 1.98%, which corresponds to 1.76, 1.63 at.%

and 1.94%, respectively. The solid solution strengthening effect due to multiple alloying elements could be described by Eq. (7) [19]

$$\sigma_s = \left(\sum_i k_i^{\frac{1}{n}} c_i\right)^n. \tag{7}$$

where n is a constant, c_i is the concentration of solute i and k_i is the strengthening constant for solute i. Ref. [19] indicated that the $n = 2/3$ was most suitable for magnesium. The contribution of Sn, Zn and Al elements on YS can be written as:

$$\Delta\sigma_s = \sigma_{s-HT} - \sigma_{s-AC}. \tag{8}$$

Due to relative low Zn and Al content, it is assumed that the Zn and Al elements are dissolved into Mg matrix, C_{Sn} is 0.86% based on the previous literature and phase diagrams [4, 19]. Thus, the $\Delta\sigma_s$ could be calculated as 13.6 MPa.

The respective contributions of grain boundary strengthening, texture strengthening, precipitation strengthening and solid strengthening to YS ($\Delta\sigma_{0.2}$) between TZA842-HT and TZA842-AC alloys were 64.5, -19, 6.4 and 19 MPa, respectively. As indicated, there is some deviation between calculated (70.9 MPa) and experimental (55 MPa) values due the deviations of the varieties and parameters used in the equations and possible defects which come from the preparation process of the alloy. Thus, it could be concluded that the grain boundary, precipitation strengthening and solid solution strengthening were the dominant strengthening mechanisms. In the case of texture strengthening, a stronger basal texture in the TZA842-AC alloy was beneficial to the YS ($\Delta\sigma_t$) but adverse to the elongation when the applied stress was perpendicular to the c-axis of the grains.

It is interesting to note that TZA842-HT exhibited better ductility than TZA842-AC, although the former exhibited higher strength than the latter. The fracture surface of the extruded alloys is shown in Fig. 7. As shown in Fig. 7a, numerous tear ridges and the particles with microcrack were present in TZA842-AC alloy, which could result in the reduction of ductility, whereas the fracture surface of the TZA842-HT alloy contained dense and finer dimples (Fig. 7b), suggesting dislocation slips were more active than the TZA842-AC, which could improve ductility [25]. Meanwhile, the TZA842-HT alloy exhibited higher work-hardening exponents (0.24) leading to a lower sensitivity to strain localization, resulted in a greater ductility. Finally, the more random texture in the TZA842-HT alloy could also lead to more dislocation slip, which tends to further increase EL [16, 26].

The aforementioned results indicated that the TZA842-HT alloy possesses a better combination of strength and ductility than the TZA842-AC does, suggesting that pretreatment is essential in improving the tensile properties of extruded Mg–Sn alloys. Thus, further research was required to determine optimal pretreatment parameters that lead to a balance of strength and production cost in extruded Mg–Sn-based alloys.

4 Conclusions

The microstructure and tensile properties of extruded TZA842 alloys subjected to AC and HT have been investigated. The main conclusions were summarized as follows:

(1) The extruded TZA842 alloy subjected to HT showed finer grain size, more uniform dispersed precipitates as well as weaker basal texture than those of counterpart subjected to AC.

(2) The TZA842-HT alloy showed higher YS of 200 MPa, UTS of 290 MPa and EL of 17.9% than those of TZA842-AC, which was mainly attributed to the combined effects of refined and homogeneous microstructure.

(3) Grain boundary, precipitation strengthening and solid solution strengthening were the dominant strengthening mechanisms in TZA842-HT alloy, while the weaker texture and a higher work-hardening exponent resulted in a greater ductility.

References

[1] W.L. Cheng, S.S. Park, B.S. You, B.H. Koo, Mater. Sci. Eng. A **527**, 4650 (2010)
[2] P. Cao, M.L. Zhang, W. Han, Y.D. Yan, L.J. Chen, Acta Metall. Sin. (Engl. Lett.) **25**, 265 (2012)
[3] W.L. Cheng, M. Wang, Z.P. Que, H.X. Wang, J.S. Zhang, C.X. Xu, B.S. You, C.D. Yim, J. Wuhan Univ. Technol. Mater Sci. Ed. **29**, 804 (2014)
[4] S. Behdad, L. Zhou, H.B. Henderson, M.V. Manuel, Y. Sohn, A. Agarwal, B. Boesl, Mater. Sci. Eng. A **651**, 854 (2016)
[5] C.Q. Liu, H.W. Chen, J.F. Nie, Scr. Mater. **123**, 5 (2016)
[6] W.L. Cheng, Y. Bai, L.F. Wang, H.X. Wang, L.P. Bian, H. Yu, Materials **10**, 822 (2017)
[7] W.J. Li, K.K. Deng, X. Zhang, K.B. Nie, F.J. Xu, Mater. Sci. Eng. A **677**, 367 (2016)
[8] K. Su, K.K. Deng, F.J. Xu, K.B. Nie, L. Zhang, X. Zhang, W.J. Li, Acta Metall. Sin. (Engl. Lett.) **28**, 1015 (2015)
[9] S.-H. Kim, S.H. Park, Mater. Sci. Eng. A **676**, 232 (2016)
[10] S.S. Park, Y.J. Kim, W.L. Cheng, Y.M. Kim, B.S. You, Philos. Mag. Lett. **91**, 37 (2011)
[11] W.L. Cheng, L. Tian, H.X. Wang, L.P. Bian, H. Yu, Mater. Sci. Eng. A **687**, 148 (2017)
[12] Q.S. Yang, B. Jiang, Z.J. Yu, Q.W. Dai, S.Q. Luo, Acta Metall. Sin. (Engl. Lett.) **28**, 1257 (2015)
[13] S.J. Meng, H. Yu, H.X. Zhang, H.W. Cui, S.H. Park, W.M. Zhao, B.S. You, Mater. Sci. Eng. A **690**, 80 (2017)
[14] C.P. Wang, H.S. Mei, R.Q. Li, D.F. Li, L. Wang, J. Liu, Z.H. Hua, L.J. Zhao, F.F. Pen, H. Li, Acta Metall. Sin. (Engl. Lett.) **26**, 149 (2013)
[15] L.F. Wang, E. Mostaed, X.Q. Cao, G.S. Huang, A. Fabrizi, F. Bonollo, C.Z. Chi, M. Vedani, Mater. Des. **89**, 1 (2016)
[16] J. Luo, H. Yan, N. Zheng, R.S. Chen, Acta Metall. Sin. (Engl. Lett.) **29**, 205 (2016)
[17] N. Tahreen, D.F. Zhang, F.S. Pan, X.Q. Jiang, C. Li, D.Y. Li, D.L. Chen, J. Alloys Compd. **615**, 424 (2014)
[18] W.N. Tang, S.S. Park, B.S. You, Mater. Des. **32**, 3537 (2011)
[19] W.L. Cheng, Q.W. Tian, H. Yu, H. Zhang, B.S. You, J. Mater. Alloys **2**, 299 (2014)
[20] H.Y. Chao, Y. Yang, X. Wang, E.D. Wang, Mater. Sci. Eng. A **528**, 3428 (2011)
[21] W. Yuan, S.K. Panigrahi, J.-Q. Su, R.S. Mishra, Scr. Mater. **65**, 994 (2011)
[22] B. Raeisinia, S.R. Agnew, A. Akhtar, Metall. Mater. Trans. A **42**, 1418 (2011)
[23] Q. Yang, F. Bu, X. Qiu, Y. Li, W. Li, W. Sun, X. Liu, J. Meng, J. Alloys Compd. **665**, 240 (2016)
[24] C.J. Wang, K.K. Deng, K.B. Nie, S.J. Shang, W. Liang, Mater. Sci. Eng. A **656**, 102 (2016)
[25] Z.T. Li, X.D. Zhang, M.Y. Zheng, X.G. Qiao, K. Wu, C. Xu, S. Kamado, Mater. Sci. Eng. A **682**, 423 (2017)
[26] B.-C. Suh, J.H. Kim, J.H. Bae, J.H. Hwang, M.-S. Shim, N.J. Kima, Acta Mater. **124**, 268 (2017)